Piezo-Polymer-Composite Unimorph Actuators for Active Cancellation of Flow Instabilities Across Airfoils

D. HALLER,[1,*] A. PAETZOLD,[2] N. LOSSE,[2] S. NEISS,[1] I. PELTZER,[2] W. NITSCHE,[2] R. KING[2] AND P. WOIAS[1]

[1]*Department of Microsystems Engineering, University of Freiburg – IMTEK, Freiburg, Germany*

[2]*Berlin Institute of Technology, Berlin, Germany*

ABSTRACT: This article presents a smart device for active cancellation of flow instabilities. An array of two piezo unimorph actuators fabricated in piezo-polymer-composite technology is combined with a thin silicone membrane to mimic a movable wall with a closed surface. By locally displacing the thin membrane, a surface wave is generated that interferes with naturally occurring flow instabilities within the boundary layer of an airfoil. Using flow sensors and an intelligent control enables a destructive interference and therefore, an attenuation of natural flow instabilities. This leads to a delay of transition. The boundary layer remains laminar which means drag is reduced. Within the next pages, the setup of the device with actuators, membrane, sensors, and control is introduced. The main focus of this article is on actuator design, modeling, and implementation for wind tunnel experiments. Results of actuator characterization are presented. The non-linear behavior of the piezoactuator (harmonic distortions and impact of high electric fields) is investigated in detail. This study concludes with the results obtained in wind tunnel experiments which prove the functionality of the presented approach. A maximal attenuation of natural occurring flow instabilities of 80% is achieved.

Key Words: actuator, piezoelectric, polymers, unimorph, harmonic distortions, active transition control, TS waves, non-linear piezoeffects, electrostriction, elastostriction.

INTRODUCTION

THE goal of this study is to conduct basic experiments which examine the possibility of an active control of boundary layer instabilities across airfoils. These instabilities occur as wave packages, so-called Tollmien–Schlichting (TS) waves. Starting as weak disturbances, the amplitudes of TS waves are increasing in downstream direction leading to a non-linear breakdown and therefore, a turbulent state (Kachanov, 1994). A turbulent boundary layer causes a significantly higher friction drag compared to a laminar boundary layer. By injecting an opposing surface wave into the laminar boundary layer, the amplitude of the TS waves can be reduced locally and hence, the transition from laminar to turbulent flow can be delayed (Thomas, 1983). Different technical approaches for active flow control are currently investigated. There are several numerical studies that use oscillating Lorentz force to manipulate turbulence structures and reduce skin friction (Berger et al., 2000; Lee and Kim, 2002). Grundmann and Tropea (2008) use pulsed plasma actuators to attenuate artificially introduced TS waves. Another possibility is to use an uncontrolled oscillating surface to reduce turbulence (Laadhari et al., 1994). Sturzebecher and Nitsche (2003) use controlled loudspeakers which displace a flexible membrane to create a counter wave in the boundary layer. Although being successful in attenuating natural TS waves, this approach is limited regarding its miniaturization potential. In order to create a traveling surface wave, an array of downstream cascaded actuators is desired. Loudspeakers cannot be cascaded as densely as required. This fact creates the need for a new, miniaturized actuator concept.

Active delay of transition demands a combined sensor–actuator system to detect the TS wave pattern and to cancel them by a suitable wave-like movement of the wing surface. Figure 1 shows the principle setup that is desired for active cancellation of boundary layer instabilities. An array of surface hot-wire sensors, placed upstream of the so-called active wall segment, detects the incoming TS waves. Downstream of the first sensor array (called reference sensor in Figure 2), an actuator system is placed. This system locally displaces an elastic membrane. The amplitude of the TS waves is amplified in downstream direction but the boundary layer in the area of the active wall segment still has to be laminar. The aim of this project is to

*Author to whom correspondence should be addressed.
E-mail: Daniel.Haller@imtek.de
Figures 1 and 3–13 appear in color online: http://jim.sagepub.com

1045-389X/11/05 0461–14 $10.00/0 DOI: 10.1177/1045389X10395794

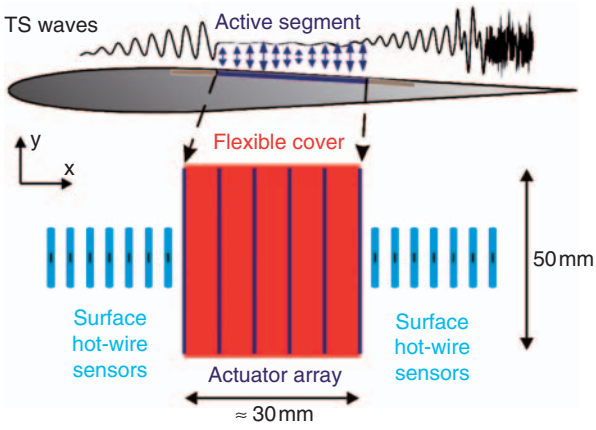

Figure 1. *Principle desired setup for active cancellation of TS waves with hot-wire sensors, elastic cover, and cascaded actuators (not to scale).*
Note: 80 × 57 mm² (300 × 300 DPI).

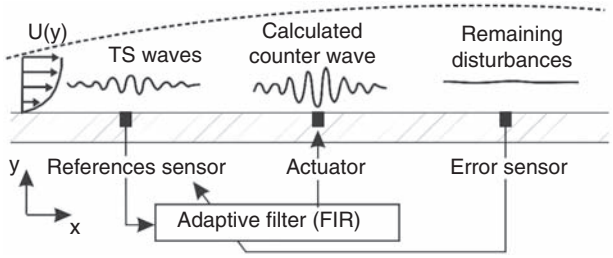

Figure 2. *Schematic of control principle (Peltzer et al., 2009).*
Note: 80 × 32 mm² (300 × 300 DPI).

induce a traveling surface wave into the boundary layer which travels with the TS waves. A traveling opposing wave is supposed to interfere with the TS waves more efficiently compared to a locally fixed induced wave. In order to induce a real traveling surface wave, several actuators, cascaded within one TS wavelength (in the performed experiments typically in the range of a few centimeters), are needed. Downstream of the actuator system at least one further sensor (error sensor) is necessary. This error sensor measures the reduction of the disturbance amplitudes and feeds back the information to the control. Figure 2 does also show a schematic of the currently used control principle. This control uses a filter-based approach (finite impulse response or FIR, explained for example by Snyder (2002)) to calculate an actuator signal that minimizes the signal amplitude of the error sensor. The FIR filter models TS-amplification, convection, and actuator response. As the TS waves occur randomly, the calculated transfer function has to be adapted continuously to achieve a suitable driving scheme for the actuator.

As a first step, a prototype, consisting of only one actuator, was developed and tested (Haller et al., 2009). The basic suitability of piezo-polymer-composite (PPC) actuators combined with the flexible silicone membrane has been proven with this prototype. In this preliminary wind tunnel experiments, natural TS waves have successfully been dampened by 42%. This article presents an enhanced device with 2 × 2 optimized unimorph PPC actuators, the next step to a cascaded actuator system. The area of the active part is increased from $6 \times 26\,\text{mm}^2$ in the prototype to $12 \times 56\,\text{mm}^2$ in the version presented here.

The purpose of this project is not to develop a device which can be used for commercial application in airplanes. The goal is to enable basic research on flow manipulation by launching counter waves into the boundary layer and to prove the principal functionality of the presented approach. For this reason, typical constraints in aerospace engineering (like weight constraints or power consumption) are not considered. The presented device has no measurable impact on the lift, as only the boundary layer of a very small part of the wing is manipulated.

PPC ACTUATOR

For the purpose of active flow control, actuators are needed which fulfill a variety of specifications. TS waves always occur as wave packages within a certain unstable frequency range (Figure 11) which is determined by the flow velocity in the wind tunnel and the pressure distribution across the airfoil. For the used low turbulent wind tunnel model and a flow velocity of 24 m/s, the unstable frequencies (TS waves) are between 200 and 600 Hz, which is, therefore, the required working range of the actuator. Within this working range, it must be possible to displace the actuator precisely and with a sufficient stroke. As the desired velocity amplitudes of the actuator are supposed to be in the range of 10% of the velocity fluctuations in the boundary layer (approximately up to 1 m/s), an actuator velocity of 0.1 m/s is required. This corresponds to an actuator stroke in the range of 100 µm at the lowest working frequency of 200 Hz. A small phase gradient within the working range is mandatory, meaning that no mechanical resonance frequency is allowed inside the working range. In order to displace the silicone membrane, the actuator has to be able to apply a sufficiently high force. The spanwise length of the active wall segment is required to be in the range of 50 mm. This is twice as large as in the preliminary setup.

The given specifications are only estimations based on previous experiments. New experiments and new insights may lead to somewhat different actuator specifications. This is one of the main reasons why the PPC technology is excellently suited for this application, as design changes can be performed rather fast and straightforward.

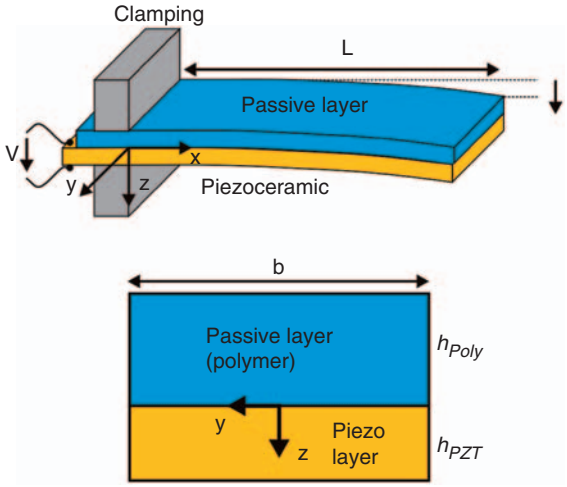

Figure 3. *Schematic of unimorph actuator: top, 3D schematic; bottom, cross-section.*
Note: 80 × 64 mm² (300 × 300 DPI).

Actuator Design and Modeling

The chosen actuator principle is a unimorph actuator made from a bilayer of a piezoceramic material and an epoxy polymer, as shown in Figure 3. Applying a voltage to the piezoceramic leads to a contraction or elongation of the ceramic material. Due to the polymer layer adhering on one side of the piezo sheet, a non-homogeneous mechanical stress distribution, and hence, a bending moment is induced into the bilayer. This leads to a vertical bending of the cantilever. For calculating the actuator static displacement, the classical laminated plate theory (CLPT) using Kirchhoff assumptions is applied (Reddy, 2004). For narrow unimorph actuators, the displacements and resultant components are independent from the y-coordinate (Yao et al., 2004a), meaning the model can be reduced to a model in which the displacement only depends on the x-coordinate. As the applied electric fields will be very high, non-linear effects in the piezoelectric material will have a significant impact on the characteristics of the unimorph (Wang et al., 1999). Therefore, these non-linear material effects have to be considered in the theory which will be used for designing the unimorph actuator. For the given case (electric field only in z-direction, no mechanical constraints in y- and z-directions), the mechanical tension in x-direction of a pure piezoceramic with applied electric field, including the non-linear material effects electrostriction and elastostriction, can be written in Voigt notation as (Joshi, 1992):

$$\sigma_1 = \frac{\varepsilon_1}{(s_{11}+\kappa_{113})E_3} - \frac{\left(d_{31}+\frac{1}{2}a_{133}E_3\right)E_3}{(s_{11}+K_{113}E_3)} = C_{11}^{*}\varepsilon_1 - X_{31}^{*}C_{11}^{*}E_3, \quad (1)$$

with d_{31} being the linear piezoelectric strain coefficient, a_{133} the electrostrictive coefficient, s_{11} the complaisant coefficient, and κ_{113} the elastostrictive coefficient. This equation can be rewritten into a more familiar version with C_{11}^{*} being a kind of effective, field-dependent stiffness including the elastostrictive effect and X_{31}^{*} an effective, field-dependent piezoelectric strain coefficient, including the electrostrictive effect. For small strains and rotations, the strain-to-displacement ratio in a cantilever is given by (Reddy, 2004):

$$\varepsilon_1 = \frac{\partial u}{\partial x} + \frac{1}{2}\left(\frac{\partial w}{\partial x}\right)^2 = \frac{\partial u_0}{\partial x} + \frac{1}{2}\left(\frac{\partial w_0}{\partial x}\right)^2 - (z-z_s)\frac{\partial^2 w_0}{\partial x^2}, \quad (2)$$

where u is the axial displacement in x-direction and w the transverse deflection in z-direction. The index 0 denotes the displacement at the neutral plane and z_s the location of the neutral plane. In the given coordinate system of Figure 3, the neutral plane depending on the effective stiffness and thus, the electric field, can be calculated as:

$$\frac{1}{2}\frac{-Y_{poly}h_{poly^2} + c_{11}^{*}h_{PZT^2}}{Y_{poly}h_{poly} + c_{11}^{*}h_{PZT}}. \quad (3)$$

The equations of motion for the considered narrow cantilever can be written in the following form (Reddy, 2004):

$$\frac{\partial N_x}{\partial x} = m^{*}\frac{\partial^2 u_0}{\partial t^2}, \quad (4)$$

$$\frac{\partial^2 M_x}{\partial x^2} + N_x\frac{\partial^2 w_0}{\partial x^2} = m^{*}\frac{\partial^2 w_0}{\partial t^2} - q, \quad (5)$$

with m^{*} being the mass resultant of inertia per length and q denoting a distributed mechanical line load. The variables N_x and M_x indicate the stress resultant and the moment resultant, respectively. They can be calculated as following, using Equations (1) and (2):

$$N_x = b\int_{-h_{poly}}^{0}\sigma_{1,poly}\,dz + b\int_{0}^{h_{PZT}}\sigma_{1,PZT}dz = A_{11}\frac{\partial u_0}{\partial x} + \frac{1}{2}\left(\frac{\partial w_0}{\partial x}\right)^2 - B_{11}\frac{\partial^2 w_0}{\partial x^2} - N_x^{p}, \quad (6)$$

$$M_x = b\int_{-h_{poly}}^{0}\sigma_{1,poly}(z-z_s)dz + \int_{0}^{h_{PZT}}\sigma_{1,PZT}(z-z_s)dz = B_{11}\frac{\partial u_0}{\partial x} + \frac{1}{2}\left(\frac{\partial w_0}{\partial x}\right)^2 - D_{11}\frac{\partial^2 w_0}{\partial x^2} - N_x^{P}. \quad (7)$$

For the given case, the extensional stiffness A_{11}, the bending–extensional coupling stiffness B_{11}, the bending

stiffness D_{11}, the actuator force resultant N_x^P and the actuator moment resultant M_x^P are:

$$A_{11} = b\left(Y_{poly}h_{poly} + C_{11}^{*}h_{PZT}\right), \tag{8}$$

$$B_{11} = b\left(Y_{Poly}h_{Poly}\left(-\frac{1}{2}h_{Poly} - z_S\right) + C_{11}^{*}h_{PZT}\left(\frac{1}{2}h_{PZT} - z_S\right)\right), \tag{9}$$

$$D_{11} = b\left(Y_{Poly}h_{Poly}\left(\frac{1}{3}h_{Poly^2} + h_{Poly}z_S + z_S^2\right) + C_{11}^{*}h_{PZT}\left(\frac{1}{3}h_{Poly^2} - h_{Poly}z_S + z_S^2\right)\right), \tag{10}$$

$$N_x^P = bX_{31}^{*}C_{11}^{*}E_3h_{PZT}, \tag{11}$$

$$M_x^P = bX_{31}^{*}C_{11}^{*}E_3h_{PZT}\left(\frac{1}{2}h_{PZT} - z_S\right). \tag{12}$$

The static displacement of a unimorph actuator can now be calculated by solving the equations of motion for static case with no external load and applying the boundary conditions of a one-sided clamped cantilever (Yao et al., 2004b). The result is:

$$w(x) = \frac{1}{2}\left(\frac{B_{11}N_x^P - A_{11}M_x^P}{A_{11}D_{11} - B_{11}^2}\right)x^2. \tag{13}$$

Putting the result for the neutral plane of Equation (3) into the expression for the bending–extensional coupling stiffness B_{11} (Equation (9)) delivers the result that B_{11} is actually 0. Thus, Equation (13) can be simplified to:

$$w(x) = \frac{1}{2}\frac{M_x^P}{D_{11}}x^2. \tag{14}$$

Calculating the eigenfrequency of the given unimorph actuator is somewhat more complex. Adjusting Equation (5) to the considered case (no external loads) delivers for the non-static case:

$$-D_{11}\frac{\partial^4 M_x^P}{\partial x^4} = m^{*}\frac{\partial^2 w_0}{\partial t^2}. \tag{15}$$

This partial derivative can be solved using a Bernoulli approach (Maurizi et al., 1976) leading to an expression for the eigenfrequency:

$$f_i = 2\pi\frac{\lambda_i}{L^2}\sqrt{\frac{D_{11}}{m^{*}}}, \tag{16}$$

where λ_i denotes the eigenvalue of the ith eigenfrequency. In this study, only the first eigenfrequency is of importance. For a cantilever clamped at one side, the first eigenvalue is 1.875. This solution only holds for a cantilever with no additional mass. An engineering approach can be used to enhance this expression for cantilevers with additional seismic mass. In this approach, the cantilever is considered as a mass–spring system. The equivalent spring constant can be approximated by calculating an equivalent force which, if applied at the tip of the cantilever, displaces the cantilever the same distance as the resulting bending moment M_x^P. The equivalent mass is the additional mass plus the mass of the cantilever. As the mass of the cantilever is distributed along the cantilever, it is not fully acting on the spring and has to be weighted with a factor smaller than 1. The resulting expression for the eigenfrequency of a unimorph actuator with additional mass at the tip is:

$$f_i = 2\pi\sqrt{\frac{k_{eff}}{m_{eff}}} = \sqrt{\frac{\frac{3D_{11}}{L^3}}{\mu_{eff}Lb\left(h_{Poly}\rho_{Poly} + h_{PZT}\rho_{PZT}\right) + m_S}}. \tag{17}$$

The coefficient μ_{eff} is determined to be 35/144 by setting the seismic mass equal to zero and comparing Equation (17) with Equation (16).

The resulting expressions of Equations (14) and (17) can now be used to find the optimum design parameters. The height of the piezoceramic (260 μm) is determined by the manufacturer. The actuator width, as long as it is in a reasonable range, has a very limited influence on the actuator displacement and resonance frequency. Therefore, the width is set to 5 mm. A larger width will not increase the actuator performance significantly, but it will increase the electric capacitance. This leaves two design parameters which can be optimized: the actuator length and the polymer layer height. Table 1 shows all the required material properties. The parameters from the polymer (an epoxy resin, Stycast 2057 from Emerson & Cumming) are determined by characterizing special test beams made only from the used polymer. The linear material constants for the used piezoceramic material (VIBRIT1100 from Johnson Matthey Catalysts) are taken from the manufacturer data sheet.

Table 1. Material properties.

Piezoceramic compliance	s_{11}	$14.2 \times 10^{-12}\,\text{m}^2/\text{N}$
Elastostrictive coefficient	κ_{113}	$-3.2 \times 10^{-18}\,\text{m}^3/\text{NV}$
Piezoelectric coefficient	d_{31}	$-315 \times 10^{-12}\,\text{m/V}$
Electrostrictive coefficient	a_{133}	$-7.5 \times 10^{-16}\,\text{m}^2/\text{V}^2$
Young's modulus polymer	Y_{Poly}	$6.64 \times 10^{9}\,\text{N/m}^2$
Density polymer	ρ_{Poly}	$1573\,\text{kg/m}^3$
Density piezoceramic	ρ_{PZT}	$8100\,\text{kg/m}^3$

The non-linear parameters are not given by the manufacturer. For the used piezoelectric material they are determined by Wischke et al. (2010).

The elastostrictive coefficient is negative, meaning that the effective stiffness is increasing with an increasing applied voltage. An increased material stiffness leads to an increased bending stiffness and therefore, according to Equation (17), an increased eigenfrequency. The electrostrictive coefficient has no influence on the eigenfrequency. The static displacement depends on both non-linear parameters. The increased material stiffness increases the bending stiffness but also the bending moment, leading to no significant impact of the elastostrictive effect on the static displacement. The electrostrictive effect increases the bending moment significantly for high applied electric fields. Depending on the geometric design parameters, the electrostrictive effect leads to a doubling of the bending moment compared to considering only linear effects (Wischke et al., 2010).

The task is not only to maximize the displacement, but also to keep the resonance frequency higher than the maximum working frequency. Figure 4 shows the static displacement according to Equation (14) plotted over the calculated eigenfrequency according to Equation (17). The applied voltage is 150 V (this corresponds to an electric field of 0.58 kV/mm), which will be the highest allowed voltage in the experiments. In Figure 4, the actuator length, as well as the polymer layer height, is varied. Each line represents a particular length with an increasing polymer layer height. The polymer layer height always starts at 100 µm for each length. Each additional marker corresponds to an additional 100 µm in the polymer layer height. Considering the displacement, there is an optimum ratio between the piezoceramic and polymer layer heights, but the eigenfrequencies are too small in this case. When looking at the maximum working frequency of 600 Hz, it becomes obvious that an increased actuator length with an increased polymer layer height leads to an increased displacement with equivalent eigenfrequency. The advantages become smaller with an increasing actuator length. For eigenfrequencies higher than the maximum working frequency of 600 Hz, there is no distinct difference between an actuator length of 30 and 35 mm. For this reason, the actuator length is set to 30 mm. The polymer layer height is chosen to be 1600 µm. The resulting analytical displacement for a voltage amplitude of 150 V is 104 µm and the eigenfrequency is 759 Hz. A safety margin of 150 Hz is added to the maximum working frequency of 600 Hz. If only linear material effects would have been considered (simply achieved by setting the electroelastic and electrostrictive coefficient to zero), the analytical displacement would be 61 µm and the eigenfrequency would be 745 Hz. The difference in the eigenfrequency is small, whereas the difference in displacement is almost 80%. The linear results match very well with 3D-finite element modeling simulations using standard simulation software (COMSOL) which considers only linear piezoelectric effects. A CAD-picture of the final design is shown in Figure 5. The final design actually consists of two unimorph cantilevers. The tips of the two cantilevers are connected *via* a 50-mm long and 0.5-mm wide polymer plunger. The plunger is needed for locally displacing the flexible cover over a longer spanwise distance.

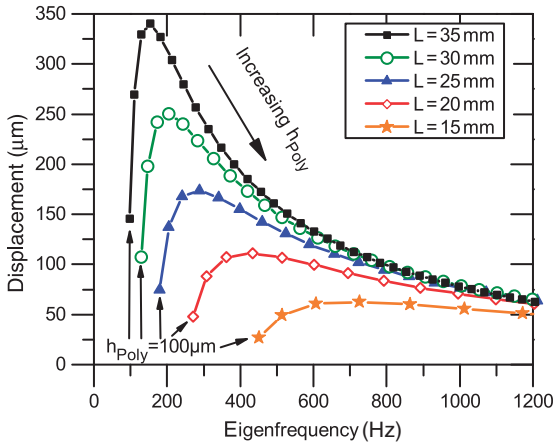

Figure 4. *Analytical displacement vs analytical eigenfrequency. Non-linear consideration with an input voltage of 150 V*
Note: 74 × 59 mm² (300 × 300 DPI).

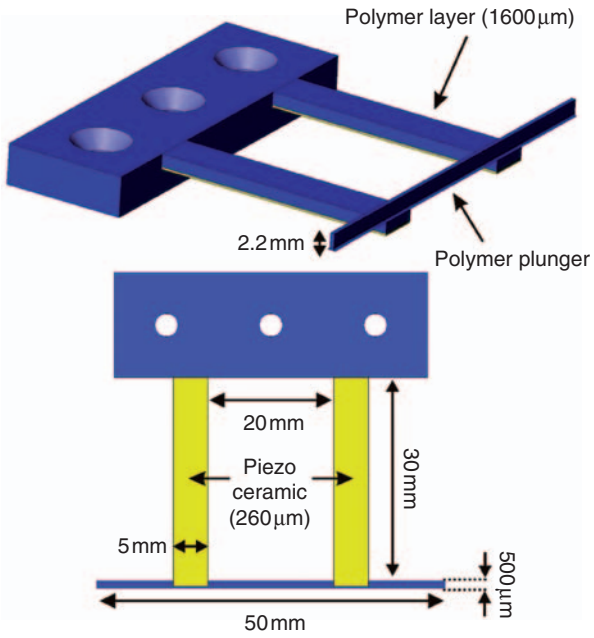

Figure 5. *Model of designed PPC actuator with two unimorph cantilevers and connecting plunger: top, 3D-view; bottom, view from beneath.*
Note: 83 × 87 mm² (300 × 300 DPI).

This rather long and fragile plunger also explains the need for having two cantilevers in parallel. The two parallel cantilevers will be connected to the same voltage source and only have the task to support the plunger at two positions in order to prevent an oscillation of the plunger. The weight of the plunger has been considered in Figure 4 according to Equation (17). Since the plunger is carried by two cantilevers, half of the mass of the plunger is added as seismic mass. Later experiments show that the individual actuator behavior does not change when the connection between the two parallel actuators is interrupted by separating the plunger. Therefore, considering the model, only one cantilever with half of the plunger is justifiable, at least as long as the two cantilevers are driven in parallel which is the case in this application. In the following chapters, the two cantilevers carrying one plunger will be denoted as one actuator.

Fabrication

As mentioned before, the developed actuators are fabricated in PPC technology. In this technology, a milled aluminum mold (positive mold), representing the geometry of the actuator, is casted with liquid silicone to replicate a negative mold. In a second step, a piezoceramic sheet is inserted into the silicone (negative) mold. Electrical connectors are also inserted into the casting mold and soldered to the piezoceramic (shown in Figure 6(a)). Next, the liquid epoxy resin is added into the silicone mold. A second half-mold is added on top and the two halves are closed together. This second silicone mold is fabricated by casting an aluminum mold that represents the plungers (Figure 6(b)). After the polymer is cured at room temperature, the fabricated actuator can now be removed from the silicone mold. The advantages of the PPC technology are a high-design flexibility and the possibility to realize design chances within a short period of time (Just et al., 2004). Using PPC technology, the very fragile plunger can be fabricated together with the actuator within the same fabrication step. Through-holes for screwing the actuator on a mount can be realized easily in PPC technology.

Actuator Characteristics

The resonance frequency of several fabricated actuators, measured at 10 V sinusoidal excitation and 0 V offset, varies between 660 and 690 Hz. This is around 10% smaller than expected from theory. There are different reasons for this behavior. First of all, the thickness of the polymer layer is reduced due to shrinkage during the curing of the polymer. The average measured thickness of the polymer layer is 60 μm thinner than the designed thickness of 1600 μm. This is a deviation of only 4%, but this deviation in the thickness reduces the analytical resonance frequency by about 30 Hz, leading to an analytical eigenfrequency of 716 Hz. Additionally, the polymer layer thickness is slightly inhomogeneous along the beam (in the range of ±20 μm) and very small air bubbles can remain inside the polymer which decreases the stiffness, as well. Furthermore, the theory assumes a perfect fixation at the clamped end of the unimorph actuator. In reality, the clamped end is not perfectly fixed. Figure 7(a) shows the actuator resonance when driven with different applied voltages. First, the amplitude is kept constant at 10 V and the offset is increased from 0 to 300 V. The increasing offset shifts the resonance frequency from 691 to 715 Hz. The analytical eigenfrequency according to Equation (17) is added in the graph. As stated above, there is a difference between analytical eigenfrequency and measured resonance frequency. In the presented case, it is 25 Hz at 0 V offset. If the analytical eigenfrequency is shifted by this constant deviation, the change of resonance frequency depending on the voltage offset is very well predicted by the presented non-linear model.

In the next experiment of Figure 7(a), the offset is kept constant at 0 V and the voltage amplitude is increased. In this case, the peak-to-peak voltage can only be increased up to $100\,V_{pp}$, as higher amplitudes lead to very high displacements at resonance which cause the actuator to break. In contrast to the previous experiment, the resonance frequency is now heavily decreasing. This behavior can be explained by two different effects. The first cause is heat generation due to loss mechanisms in the piezoceramic (Uchino et al., 2006). The higher the voltage amplitude becomes, the higher the generated heat and, therefore, the actuator temperature becomes. In the performed experiments, the actuator temperature at the bearing reached up to 35°C at the highest applied voltage in resonance. The increased temperature leads to a reduced material stiffness, especially of the polymer layer. The second, and more dominating effect decreasing the actuator's resonance frequency is a non-linear restoring force and spring constant. A unimorph actuator is a non-linear oscillator, also called Duffing oscillator. This means the spring constant depends on the displacement and thus, also the dampening constant of the unimorph actuator. The displacement magnification in resonance of unimorph actuators decreases with an increasing electric field. This means the dampening constant is increasing and the quality factor is decreasing (Wang et al., 1999). A higher dampening constant leads to a larger difference between eigenfrequency and resonance frequency. Therefore, the resonance frequency decreases with an increasing applied voltage amplitude. Since the presented non-linear theory only calculates the eigenfrequency, this fact cannot be considered in the theory.

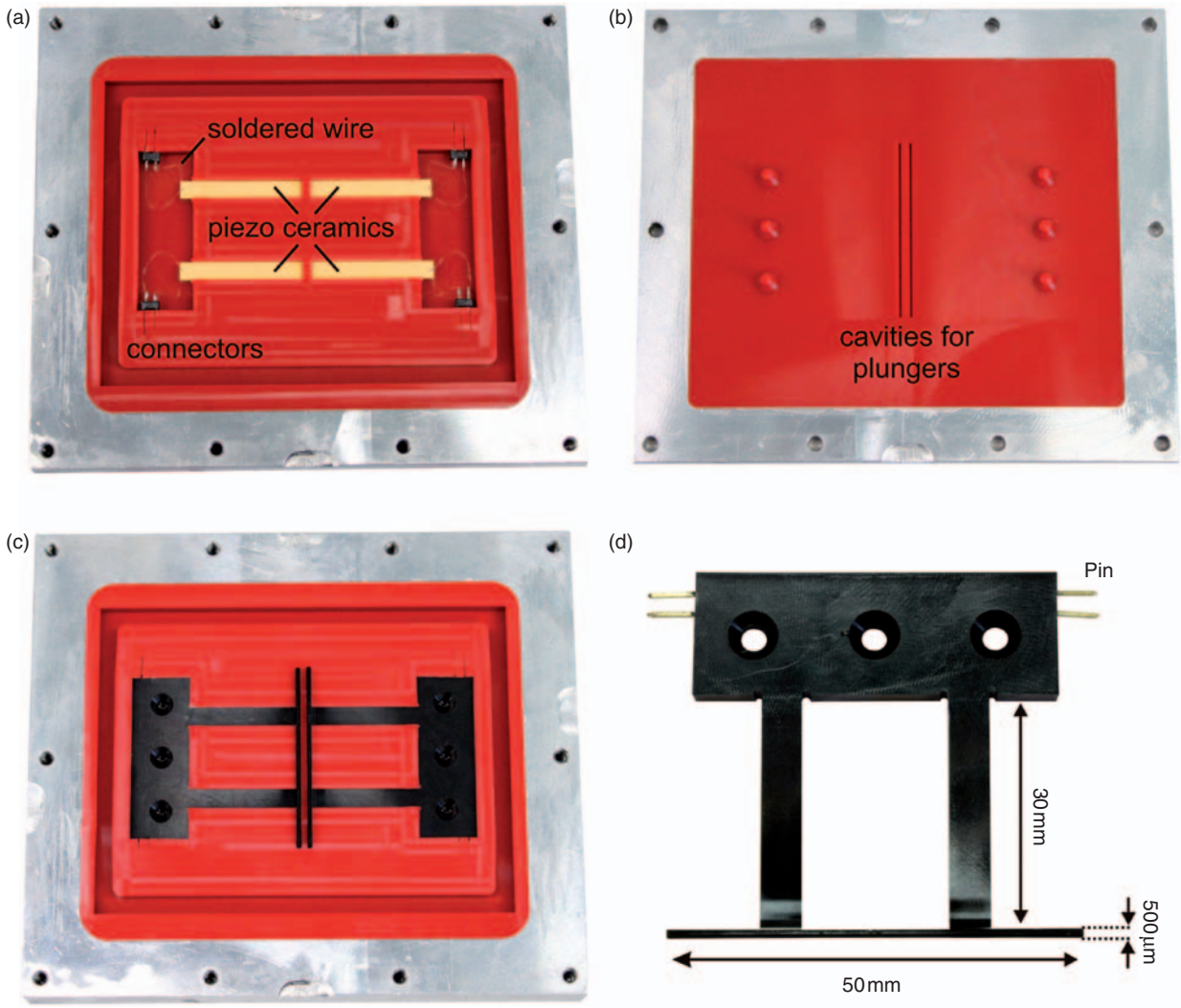

Figure 6. *Different fabrication steps of a PPC actuator. In the shown mold, two actuators can be casted at the same time. (a) Bottom silicone mold (negative) with inserted and connected piezo sheets; (b) upper silicone mold (negative); (c) PPC actuators in silicone mold after curing; and (d) casted PPC unimorph actuator.*
Note: 154 × 134 mm² (300 × 300 DPI).

The measured static displacement at 150 V amplitude with an offset of 50 V is between 115 and 120 µm, which is slightly higher than expected from theory. With the real measured thickness, the analytical displacement is around 109 µm. The remaining difference can be explained with inaccuracies in the material properties, especially in the electrostrictive coefficient. This material property heavily depends on the driving condition or in other words, the state of absolute polarization (Wischke et al., 2010). The measured frequency response of the fabricated actuator is shown in Figure 7(b). Several steps are necessary to obtain this graph. First, the frequency response is measured applying a voltage amplitude of 50 V with a 20 V offset. Due to the resonance magnification and the low dampening constant ($D \approx 0.016$), the displacement is significantly increased for frequencies above 450 Hz. This would lead to a damaging of the actuator when applying a high voltage, single-frequency sine wave with frequencies higher than 450 Hz. Therefore, the transfer function between input voltage and measured displacement is calculated from the measured data for 50 V. The inverse of this transfer function is then applied to the input voltage when driving the actuator with an amplitude of 150 V and a 50-V offset. This compensates for the frequency magnification and prevents a damaging of the actuator. The dashed lines represent the displacement when actuating a 90-µm thick, 10% pre-stressed silicone membrane. The displacement is somewhat reduced (approximately 15% in both cases), but the requirement of 100 µm stroke is still fulfilled. The membrane increases the resonance frequency by 20 Hz.

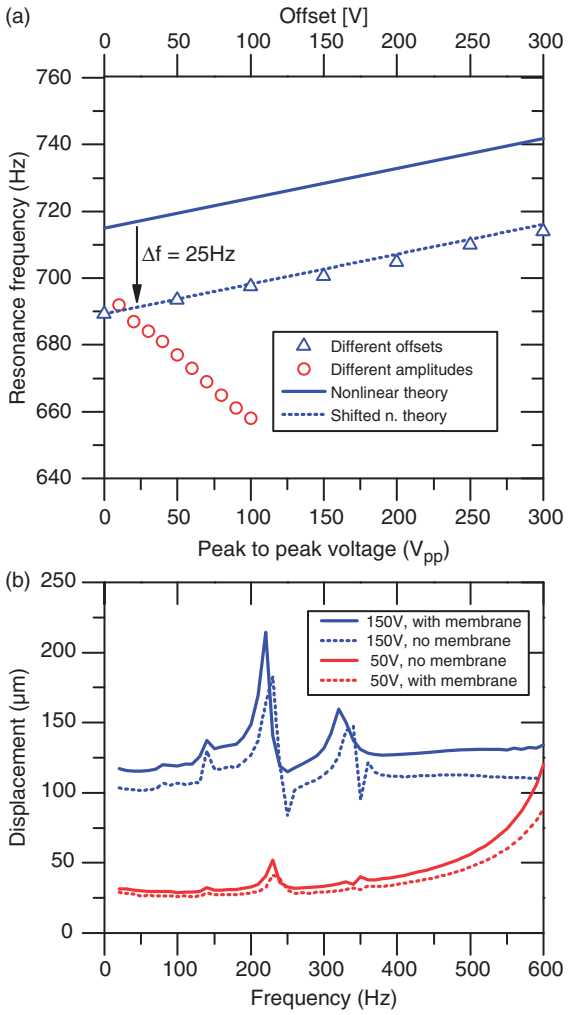

Figure 7. *(a) Analytical eigenfrequency and measured resonance frequencies for different offsets at a constant amplitude of 10 V (triangles) and for different peak-to-peak voltages at a constant offset of 0 V (circles). (b) Maximum tip displacement of a fabricated PPC actuator without and with 10% pre-stressed membrane. Note: 74 × 136 mm² (300 × 300 DPI).*

All graphs of Figure 7(b) show a distorted behavior for frequencies up to almost 400 Hz. The displacement is distorted around multiple integer divisors of the actuator resonance frequency. The distortions are much larger at the higher voltage measurement. The reason for this behavior is mostly based on the non-linear effects in piezoelectric materials (hysteresis between voltage and strain, electrostriction, and elastostriction). In piezoceramics, polarization, and therefore, charge is the actual driving value. When driving the piezo actuator with a single frequency and perfectly sinusoidal input voltage, the hysteresis effect leads to a slightly distorted input current (Figure 8(a) and (b)). The current signal now contains additional harmonic oscillations at integer multiple frequencies of the excitation frequency. These oscillations are at least 20 dB smaller compared to the main oscillation. However, if one of the additional higher harmonic oscillations coincides with the resonance frequency or frequencies close to the resonance frequency of the actuator, it is mechanically amplified and becomes visible in the actuator displacement. Figure 8 shows the actuator behavior when applying a sinusoidal voltage with a frequency of one-third of the resonance frequency. The peak in the displacement spectrum (Figure 8(d)) at twice the excitation frequency is visible, but small compared to the excitation frequency. The peak at three times the excitation frequency is mechanically amplified as it coincides with the resonance frequency. This peak is not negligible small any more. Thus, the excited oscillation is superposed with the mechanical resonance frequency, which can be seen in the time plot of Figure 8(c). This phenomenon is called harmonic distortion (Royston and Houston, 1998). Any non-linearity between input signal and resulting displacement will cause harmonic distortions. Using a charge driver instead of a voltage driver would reduce the harmonic distortions caused by the electric field to polarization hysteresis. The harmonic distortions caused by non-linear material effects like electrostriction and elastostriction would remain. Mechanical non-linearities, if present, will also lead to harmonic distortions. The non-linear change of the dampening constant cannot be definitely allocated to a solely electrical- or mechanical-based physical cause. However, it also has an impact on the dynamic behavior of the actuator.

At 150 V, the distortions are much more significant than at 50 V. The hysteresis loop which has to be passed is larger and the electrostrictive effect is more significant. Adding the membrane reduces the effect. The membrane increases the mechanical dampening constant and therefore, decreases the resonance magnification. The mechanical amplification becomes smaller. Additionally, the distortions are slightly shifted to higher frequencies, as the resonance frequency is increased by the membrane.

SYSTEM IMPLEMENTATION

Two of the introduced PPC actuators are mounted onto a heavy brass mount with their plungers facing each, as shown in Figure 9. Two slightly different setups are investigated. The only difference in the setups is the distance between the two actuators. In the first setup, the distance between the actuators is 6 mm, whereas in the other setup, the distance is decreased to 3 mm. These two setups are intended to answer the question whether an actuator distance of 6 mm is sufficient, or if a further reduction of the distance is enhancing the dampening capability of the system. A 90-µm thick silicone membrane is clamped into an aluminum mount which is attached on the brass mount, as well. The inner size of the membrane mount is adjusted to the

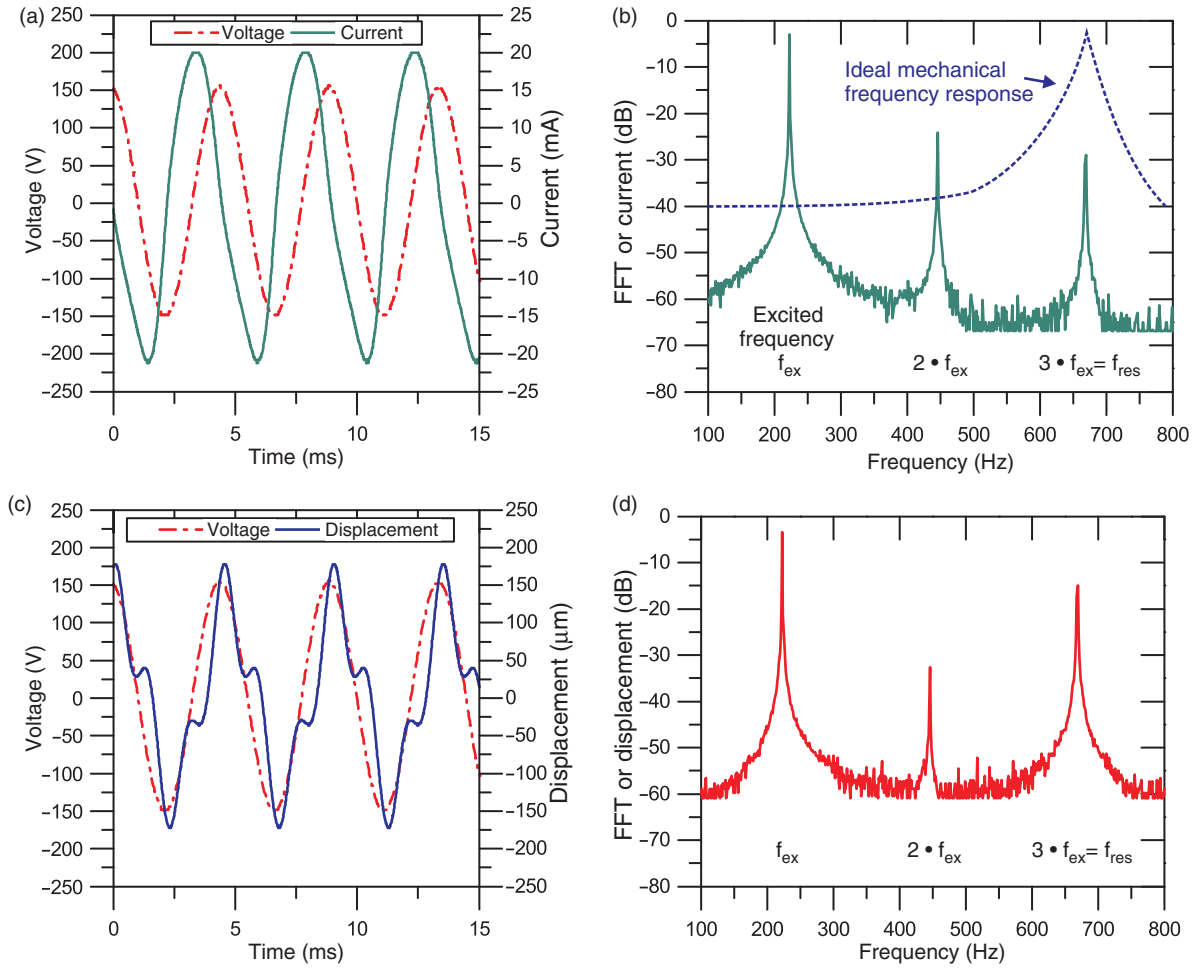

Figure 8. *Measured harmonic distortion phenomenon at a piezoelectric unimorph actuator when excited with a single frequency sine wave at one-third of the resonance frequency ($f_{ex} = 223$ Hz, $U_{amp} = 150$ V): (a) time plot of applied voltage and measured resulting current; (b) frequency spectrum of the current signal plus frequency response of an ideal actuator with mechanical resonance at 670 Hz; (c) time plot of applied voltage signal and resulting actuator displacement; (d) frequency spectrum of the distorted actuator displacement.*
Note: 156 × 127 mm² (300 × 300 DPI).

actuator distance. The distance from the inner edge of the membrane mount to the closest edge of the plungers is 3 mm, all around. The outer dimensions of the two different membrane mounts for the two different actuator distances are the same. The membrane is glued onto the plungers and can now be considered as an active wall segment. The overall area of the active wall segment is $56 \times 9\,\text{mm}^2$ for the 3-mm distance setup and $56 \times 12\,\text{mm}^2$ for the 6-mm distance setup. Before clamping the membrane, a pre-stress with an elongation of 10% is applied. Otherwise, the membrane would be too soft, which could lead to an overshooting of the membrane segment between the two plungers.

An aluminum insert is used to implement the system into the wind tunnel setup. This insert has an opening in the center that carries a printed circuit board (PCB). The brass mount is screwed to the aluminum insert from underneath. The PCB has a rectangular opening, as well, with dimensions that are 100 µm larger than the membrane fixation. Since the outer dimensions of the two different membrane mounts are equivalent, the same PCB can be used for both actuator distances. Additionally, the PCB has 20 pairs of structured electrodes, 10 pairs upstream, and 10 pairs downstream of the active wall segment. Surface hot-wire sensors with a diameter of 5 µm are welded across small cavities between one pair of electrodes (see detailed view in Figure 9(c)). The task of the sensors is to detect the small flow fluctuations of the TS waves within the boundary layer. The reduction of these fluctuations is a measure for determining the success of the flow manipulation experiment. The distance between the sensors is 5 mm. Constant temperature anemometry is used as measurement technique and a digital signal processor (DSP) enables a fast acquisition of the sensor data. The high quality of the applied sensor technology and acquisition method has already been presented in several works and publications from the project partners

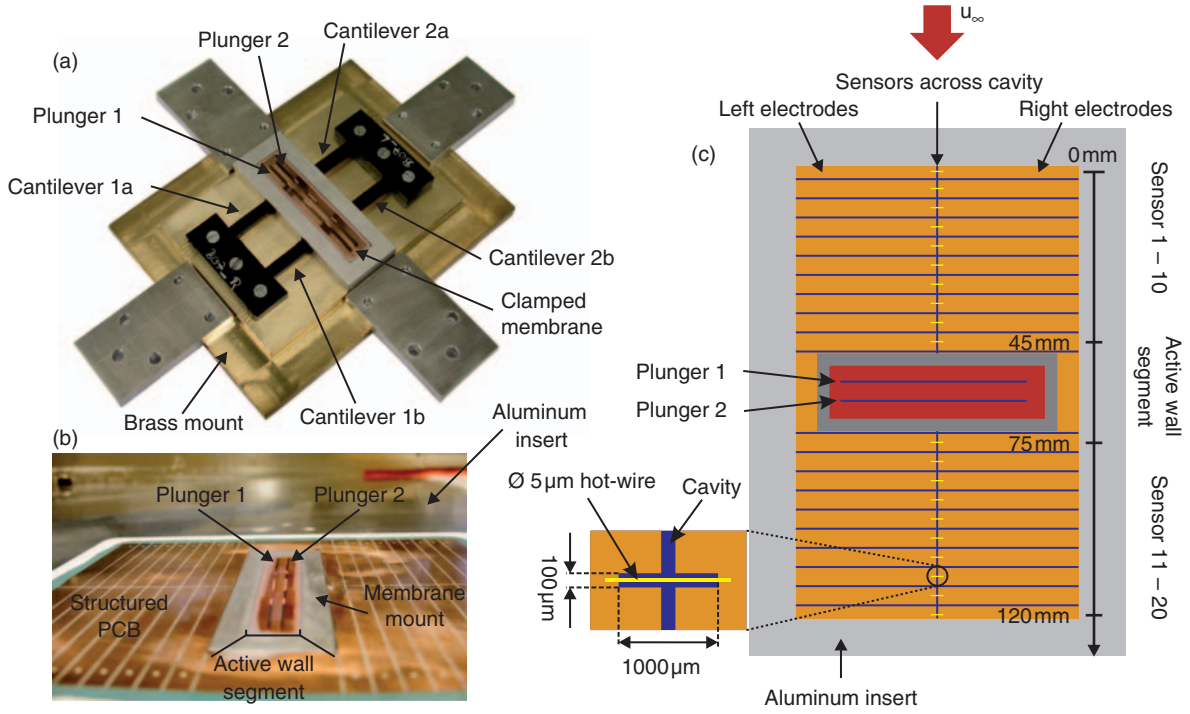

Figure 9. *Various steps of system implementation; (a) two PPC actuators with clamped membrane on the brass mount; (b) aluminum insert and laminated PCB with hot-wire flow sensors and active wall segment; and (c) schematic with a detail view on the hot-wire sensor configuration. Note: 168 × 100 mm² (300 × 300 DPI).*

(e.g. Sturzebecher et al., 2001). The sensors are not calibrated, but adjusted for equal sensitivity. The control requires only two sensors (error and reference sensors), but for evaluating the local development of TS waves and the influence of the active control further downstream, 20 sensors are implemented in the setup.

It is very important to mechanically decouple the actuators from the sensors. The actuators are very strong and if they would directly touch the PCB, they would set the PCB and hence, the sensors, into a mechanical vibration when turned on. This mechanical coupling is prevented by using the heavy brass mount. The aluminum insert can be implemented into an airfoil model. For active wave cancellation, a smart control is essential. The control has to evaluate the sensor signals and to calculate the appropriate driving signals for the actuators. In this setup, a DSP reads the sensor signals and drives the actuators. A high-voltage amplifier is employed to create the needed driving voltages. The presented results are gained by using the filter-based control (FIR), introduced in the first section. The signal of the error sensor is minimized using a least mean square algorithm. This control is not able to drive separate actuators individually from each other. Therefore, the two actuators are driven in parallel in the presented experiments. The generated opposing counter wave is not a traveling wave, yet. In order to drive cascaded actuators individually, a more intelligent control scheme is currently being developed. This new control is called model predictive control (MPC, King et al., 2008). The MPC is able to predict the downstream progression of the incoming TS waves and to calculate the required opposing traveling wave of the actuator system considering only the upstream sensor signals (reference sensor). Using this enhanced control will enable to create a real traveling opposing wave in future experiments.

WIND TUNNEL EXPERIMENTS

The basic suitability of PPC actuators combined with a silicone membrane for active cancellation has already been successfully proven in previous experiments (Haller et al., 2009). Using one single PPC actuator and a $26 \times 6\,\text{mm}^2$ large membrane, in combination with the same sensors and control, enabled a dampening of TS waves of 42%. The experimental results using the device introduced in this article with an actuator distance of 6 mm are presented in Figures 10 and 11. The used wind tunnel is a low turbulence wind tunnel with a turbulence level between 0.2% and 0.6%. The airfoil is an unswept, symmetrical 2D one (model NACA0008 with a cord of 1300 mm and a span of 600 mm). The wind tunnel velocity for all experiments is 24.5 m/s, which

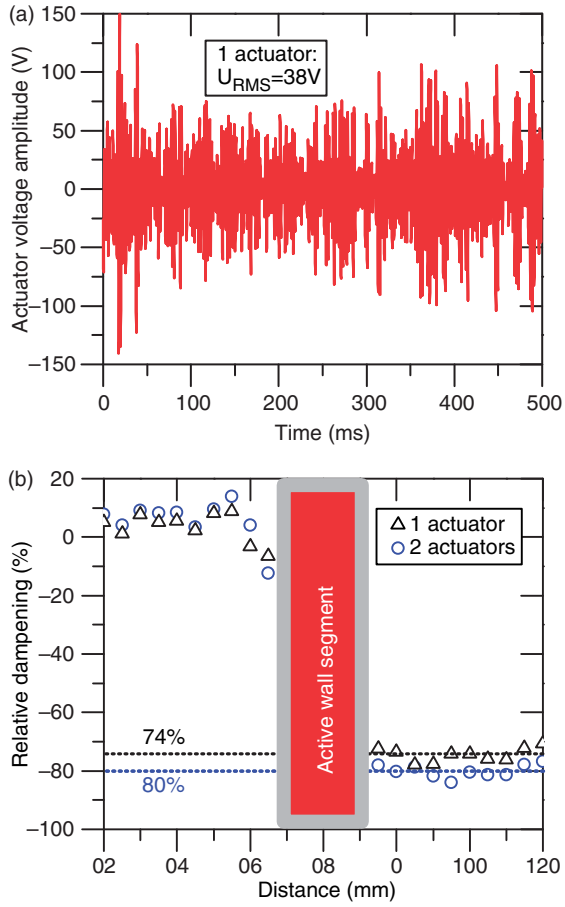

Figure 10. *Sensor signals of 20 surface hot-wires for natural flow compared to flow with active control using only one actuator or both actuators in parallel with 6 mm distance; top: RMS values; bottom: relative damping of RMS value.*
Note: 75 × 128 mm² (300 × 300 DPI).

corresponds to a Reynolds number of around one million. The angle of attack is adjusted in such a way that the active segment is located in the transition regime where the TS waves are already amplified, but the boundary layer is still laminar. This is achieved with an angle of attack at around 0°. The top graph of Figure 10 shows the root mean square (RMS) values of all 20 surface hot-wire sensors for natural flow and for a flow with active control using only one actuator or both actuators in parallel. The surface hot-wire sensors, which actually measure temperature fluctuations, are not calibrated. Therefore, all sensors were first adjusted to a similar sensitivity by applying a turbulent flow and normalizing the measured values. In the case of the natural flow, the RMS values are increasing from sensor 1 to sensor 20, i.e. the amplitude of the TS waves is increasing. The RMS values of the flow sensors indicate the size of the mean velocity fluctuations of the TS waves. The larger the mean velocity fluctuations are, the less laminar the boundary layer is. The increase of the RMS values is not smooth and does have some small spikes. This can be caused by a remaining difference of the sensor sensitivities. In this experiment, the overall distance from sensor 1 to sensor 20 is 120 mm ($19 \times 5\,\text{mm}^2 + 25\,\text{mm}$) with sensors 1–10 located upstream and sensors 11–20 located downstream of the active wall segment. Activating the flow control clearly reduces the RMS values of the downstream sensors for both cases. The average dampening of the downstream sensors is 74% using only one actuator and 80% using both actuators in parallel, as shown in the bottom graph of Figure 10. The upstream effect of the actuators is very small and only observable in the sensors very close to the active wall segment.

Figure 11 presents the frequency spectra of sensor 10 (last sensor upstream of the active wall segment), sensor 11 (first sensor downstream of the active wall segment), and sensor 20 (most downstream sensor) of the experiment using both actuators in parallel with a 6 mm distance. The spectra of the dampening results using only one actuator are not presented here in detail, but they show, besides the slightly smaller dampening, a very similar behavior. Again, natural flow is compared to dampened flow with active control. The spectra of the natural flow show the typical amplification of natural TS waves. The unstable frequency range (fundamental TS waves) is between 200 and 650 Hz and the disturbance is increasing in downstream direction. When the disturbances reach a certain size, higher harmonics of the TS waves can be observed in the spectra (700–1100 Hz). At 560 Hz, an obvious peak exists in all spectra. This peak is caused by the wind tunnel itself and is therefore called wind tunnel noise. Despite the slight reduction of the RMS value of sensor 10, no differences in the spectrum of natural flow compared to flow with active control can be observed. In the spectrum of sensor 11, the active control influence is distinct. The spectral components from 350 to 600 Hz are significantly reduced. When looking at the frequency range between 650 and 700 Hz, the active control increases the spectral components, visible at sensor 11. This behavior is the consequence of the harmonic distortions of the actuator, explained in the previous chapter. However, in the spectrum of sensor 20, these spectral components have almost completely disappeared. Frequencies between 650 and 700 Hz are not unstable frequencies of the flow and are, therefore, dampened by the flow itself. The second frequency range with increased spectral components between 700 and 1100 Hz has also disappeared at sensor 20. Since the size of the fundamental TS waves has been reduced, the higher harmonics are reduced, as well.

Between 200 and 350 Hz, almost no influence can be observed. At lower frequencies, larger displacement amplitudes are needed to get the same velocity amplitudes. This leads to the conclusion that the actuator

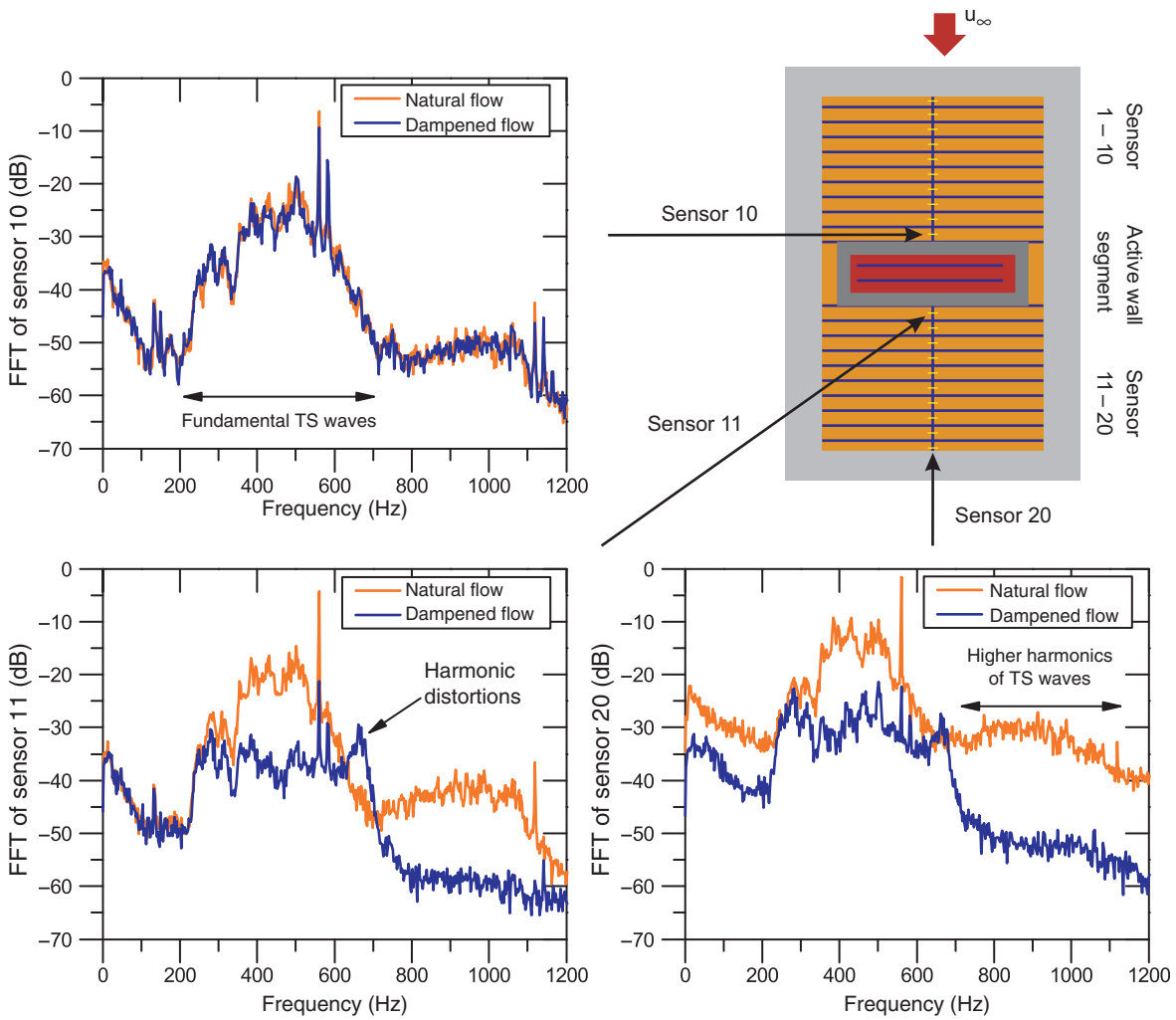

Figure 11. *Frequency spectrum of sensor 10 (5 mm upstream of active wall segment), sensor 11 (5 mm downstream of active wall segment), and sensor 20 (50 mm downstream of active wall segment). The results are taken from the experiment with 6 mm actuator distance and using both actuators in parallel.*
Note: 153 × 134 mm² (300 × 300 DPI).

stroke seems to be not sufficiently high, but this assumption is disproved by looking at the actuation voltage, presented in Figure 12. The control is allowed to increase the voltage up to a maximum limit set to ±150 V (the 50 V constant offset is added afterward). In fact, the applied voltage of the control never crossed ±60 V when using both actuators. In principle, the actuator would be able to deliver a higher stroke, but the control does not demand a higher actuator stroke. Therefore, the control has to be improved, as the actuator performance is not limiting the dampening capability of the system. Comparing the actuation voltages using one or two actuators shows that the required actuation voltage, and hence, the required actuator stroke, is smaller when using both actuators. The effective voltage is reduced from 38 to 29 V. The maximum required voltage during the full 5-s long recorded actuation signal is reduced from 150 V using one actuator to slightly above 60 V using both actuators.

In comparison to the above-presented results, the setup with a 3-mm actuator distance shows a very similar behavior and is therefore not shown in detail, here. The mean dampening of the RMS values is 72% using both actuators in parallel. This is slightly worse as the dampening results of the setup with 6 mm distance between the actuators. The spectra of the dampened flow show the same characteristics (good dampening for higher frequencies and almost no dampening for frequencies below 350 Hz) and the maximal required actuation voltage is also 60 V. The dampening capability is not enhanced by reducing the actuator distance from 6 to 3 mm.

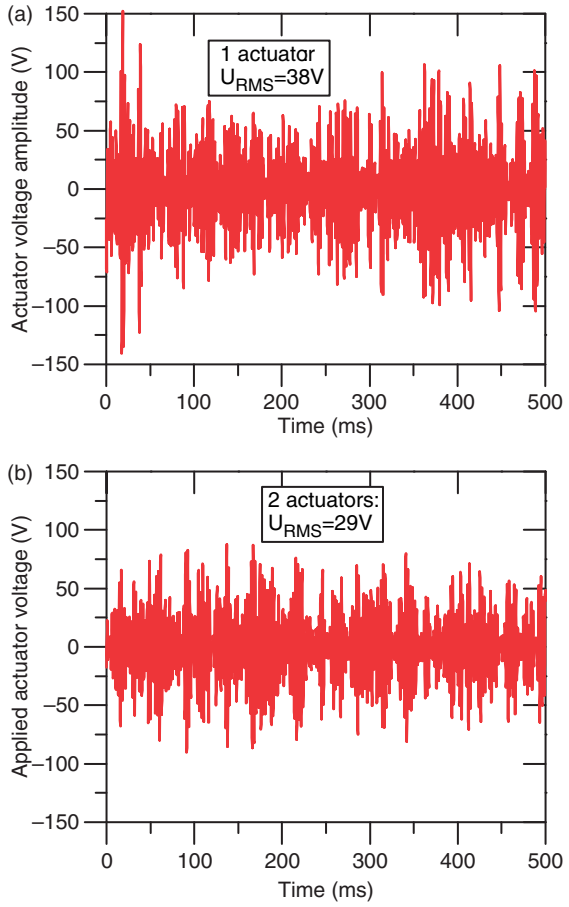

Figure 12. *Applied actuation voltage using only one actuator (top, 74% dampening) or both actuators in parallel (bottom, 80% dampening).*
Note: 76 × 122 mm² (300 × 300 DPI).

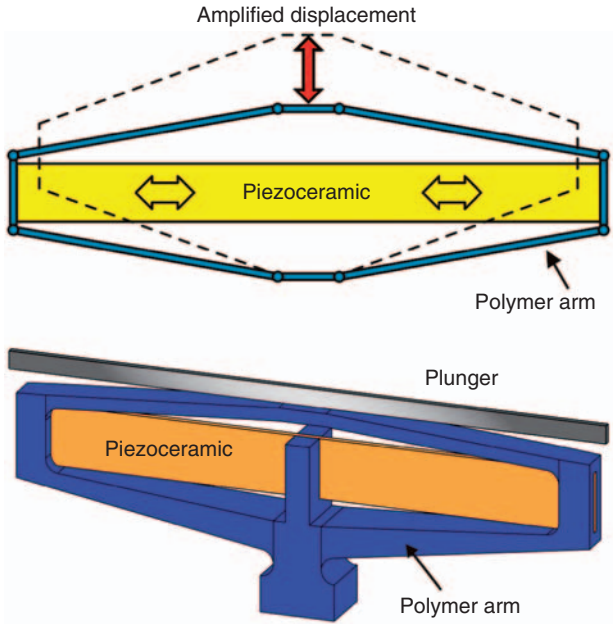

Figure 13. *Cymbal actuator; top: working principle; bottom: 3D-CAD simulation model.*
Note: 80 × 82 mm² (300 × 300 DPI).

CONCLUSION AND OUTLOOK

The developed non-linear actuator model, considering the electrostrictive and the elastostrictive effects, enabled an appropriate design and optimization process for the required unimorph actuators. On the one hand, the measured actuator characteristics correspond very well to the predicted actuator behavior. On the other hand, the developed unimorph actuators show some additional dynamic non-linearities, mainly the so-called harmonic distortions. This effect can be explained by the static non-linearities of the piezoelectric material.

The developed actuator is combined with a silicone membrane and implemented into a wind tunnel setup. The dampening capability of the full setup is successfully proven in wind tunnel experiments. Using two cascaded actuators and increasing the area of the active wall segment in spanwise and in downstream direction enhanced the dampening of natural TS waves from 42% using the preliminary setup up to 80% when evaluating the new developed setup with twice the dimension in spanwise direction and two cascaded actuators. When disconnecting the second actuator and driving only one actuator, the dampening capability is somewhat reduced (74%). This proofs that injecting the counter wave over a larger area is advantageous for dampening the TS waves. The individual required actuator stroke of each actuator is smaller when two actuators are used. The applied maximum actuation voltages in the different dampening experiments correspond to an actuator stroke of around 40 µm using both actuators and 100 µm using only one actuator. The experiments show that the actuator performance is sufficient for the application and the system implementation has proven to be successful. A further optimization of the actuator stroke will not lead to an improvement in dampening the TS waves as already only a part of the full possible actuator stroke is required by the control. TS waves with high frequencies have been dampened very well. In contrast, TS waves with low frequencies have been attenuated very little. This leaves room for optimization. An increased active area should in principle be able to inject a surface wave with a larger wavelength. This should enhance the dampening of low frequency TS waves. Additionally, based on the experimental results, an even larger active area is supposed to require an even smaller individual actuator displacement. This is an important insight regarding the development of an actuator concept which is suitable for numerous cascading in the required distances. Harmonic distortions caused by the non-linear effects of the piezoelectric material does influence the boundary layer but in an acceptable way. Two basic steps are necessary to further improve this project. First of all, the MPC has to be established, to generate a real traveling wave instead of a locally fixed wave. The second step is to develop an actuator design

that allows to cascade more than two actuators with only a few millimeters distance in between. Unimorph actuators are not suitable for cascading, as the cantilevers need too much lateral space. The actuator principle that is currently used for developing the next actuator generation is the so-called Moonie or Cymbal structure (Dogan et al., 1996). Figure 13 shows the basic idea of this kind of piezo actuator fabricated in PPC technology. Instead of having a lateral composite cantilever, two truncated and V-shaped bars are vertically connected with a piezoceramic beam. The bars amplify the horizontal piezo movement in vertical direction. Such actuators can also be fabricated in the introduced PPC technology, but the design process is more complicated. However, using this actuator principle will enable to cascade as many actuators as necessary with a distance down to 5 mm between the actuators. The experimental results show that decreasing the actuator distance from 6 to 3 mm does not enhance the dampening capability. Therefore, the possible minimal cascading distance of Cymbal type actuators of 5 mm is sufficient.

ACKNOWLEDGMENT

We gratefully acknowledge the "German Research Foundation" (DFG) for financial support within the priority program 1207, "Nature Inspired Fluid Dynamics."

REFERENCES

Berger, T.W., Kim, J., Lee, C. and Lim, J. 2000. "Turbulent Boundary Layer Control Utilizing the Lorentz Force," *Physics of Fluids*, 12:632–649.

Dogan, A., Fernandez, J.F., Uchino, K. and Newnham, R.E. 1996. "The "Cymbal" Electromechanical Actuator," In: *Proceedings of the Tenth International Symposium on Applications of Ferroelectrics*, 18–21 August, Vol. 1, IEEE Press, East Brunswick, pp. 213–216.

Grundmann, S. and Tropea, C. 2008. "Active Cancellation of Artificially Introduced Tollmien–Schlichting Waves Using Plasma Actuators," *Experimental Fluids*, 44:795–806.

Haller, D., Hempel, J., Pätzold, A., Losse, N., Peltzer, I., Nitsche, W., King, R. and Woias, P. 2009. "A Piezo Actuated Closed Loop MEMS System for Active Delay of Transition," In: *Digest Tech. Papers Transducers'09 Conference*, 21–25 June, Denver, pp. 1533–1536.

Just, E., Bingger, P. and Woias, P. 2004. "Piezo-Polymer-Composite Actuators – A New Chance for Applications," In: *Digest Tech. Papers Actuator 04*, 14–16 June, Bremen, pp. 521–524.

Joshi, S.P. 1992. "Nonlinear Constitutive Relations for Piezoceramic Materials," *Smart Materials and Structures*, 1:80–83.

Kachanov, Y.S. 1994. "Physical Mechanism of Laminar-Boundary-Layer Transition," *Annual Review of Fluid Mechanics*, 26:411–482.

King, R., Aleksic, K., Gelbert, G., Losse, N., Muminovic, R., Brunn, A., Nitsche, W., Bothien, M.R., Moeck, J.P., Paschereit, C.O., Noack, B.R., Rist, U. and Zengl, M. 2008. "Model Predictive Flow Control," In: *Invited Paper for 4th Flow Control Conference 2008*, 23–25 June, Seattle, pp. 1–19.

Laadhari, F., Skandaji, L. and Morel, R. 1994. "Turbulence Reduction in a Boundary Layer by a Local Spanwise Oscillating Surface," *Physics of Fluids*, 6:3218–3220.

Lee, C. and Kim, J. 2002. "Control of the Viscous Sublayer for Drag Reduction," *Physics of Fluids*, 14:2523–2529.

Maurizi, M.J., Rosii, R.E. and Reyes, J.A. 1976. "Vibration Frequencies for a Uniform Beam With One End Spring-Hinged and Subjected to a Translational Restraint at the Other End," *Journal of Sound and Vibration*, 48:565–568.

Peltzer, I., Paetzold, A. and Nitsche, W. 2009. "In-flight Experiments for Delaying Laminar-Turbulent Transition on a Laminar Wing Glove," *Proceedings of IMechE, Part G, Journal of Aerospace Engineering*, 223:619–626.

Reddy, J.N. 2004. *Mechanics of Laminated Plates and Shells: Theory and Analysis*, 2nd edn, CRC Press, Boca Raton.

Royston, T.J. and Houston, B.H. 1998. "Modeling and Measurement of Nonlinear Dynamic Behavior in Piezoelectric Ceramics with Application to 1-3 Composites," *Journal of Acoustic Society of America*, 104:2814–2827.

Snyder, S. 2002. *Active Noise Control Primer*, Springer Verlag, New York, Berlin.

Sturzebecher, D., Anders, S. and Nitsche, W. 2001. "The Surface Hot Wire as a Means of Measuring Mean and Fluctuating Wall Shear Stress," *Experiments in Fluids*, 31:294–301.

Sturzebecher, D. and Nitsche, W. 2003. "Active Cancellation of Tollmien-Schlichting Instabilities on a Wing Using Multi-channel Sensor-Actuator Systems," *International Journal of Heat and Fluid Flow*, 24:572–583.

Thomas, A.S.W. 1983. "The Control of Boundary Layer Transition Using a Wave Superposition Principle," *Journal of Fluid Mechanics*, 137:233–250.

Uchino, K., Rajapurkar, A., Zhuang, Y., Ural, S. and Park, S. 2008. "High Power Piezoelectric Components," In: *Digest Tech. Papers Actuator 08*, 9–11 June, Bremen, pp. 52–55.

Wang, Q., Zang, Q., Xu, B., Liu, R. and Cross, E. 1999. "Nonlinear Piezoelectric Behavior of Ceramic Bending Mode Actuators Under Strong Electric Fields," *Journal of Applied Physics*, 86:3352–3360.

Wischke, M., Haller, D., Goldschmidtboeing, F. and Woias, P. 2010. "Assessing the Elastostriction and Electrostriction Parameters of Bulk PZT Ceramics," *Smart Materials and Structures*, 19:085003.

Yao, L.Q., Zhang, J.G., Lu, L. and Lai, M.O. 2004a. "Nonlinear Dynamic Characteristics of Piezoelectric Bending Actuators Under Strong Applied Electric Field," *Journal of Microelectromechanical Systems*, 13:645–652.

Yao, L.Q., Zhang, J.G., Lu, L. and Lai, M.O. 2004b. "Nonlinear Static Characteristics of Piezoelectric Bending Actuators Under Strong Applied Electric Field," *Sensors and Actuators A*, 115:168–175.